

A photonic interface of chiral cavity quantum electrodynamics

Fan Zhang,¹ Lingxiao Shan,¹ Juanjuan Ren,¹ Xueke Duan,¹
Yan Li,^{1,2} Tiancai Zhang,^{2,3} Qihuang Gong,^{1,2} Ying Gu^{1,2*}

¹State Key Laboratory for Mesoscopic Physics, Collaborative Innovation Center of Quantum Matter, Department of Physics, Peking University, Beijing 100871, China

²Collaborative Innovation Center of Extreme Optics, Shanxi University, Taiyuan, Shanxi 030006, China

³State Key Laboratory of Quantum Optics and Quantum Optics Devices, Institute of Opto-Electronics, Shanxi University, Taiyuan 030006, China

*ygu@pku.edu.cn.

Cavity quantum electrodynamics studies light-matter interactions at single quanta level. Chiral photon-emitter coupling in photonic structures is characterized as unidirectional propagation locked by the local polarization of light. However, to realize the strong interaction of photon-emitter with direction-locked propagation, which will bring novel applications in nonreciprocal quantum devices, has not been reported yet. Here, we propose the coupled photonic crystal and metallic nanoparticle structure, where through strong local field with high helicity, the rate of circularly polarized photons emitting into photonic crystal waveguide is one order larger than that without the nanoparticle and the linewidth of Rabi splitting spectra is about one-tenth of that with only the nanoparticle, both with $\sim 95\%$ photons propagating unidirectionally, which can be utilized in directional quantum light sources.

Cavity quantum electrodynamics (CQED) studies the light-matter interaction at a single quanta level (1, 2). With confined electromagnetic fields, optical mode volume and mode density determine the behavior of photon-emitter coupling. In traditional CQED, by compressing the optical mode volume into the region of several hundreds of micrometers, weak and strong couplings have been achieved (3). In weak coupling regime, the spontaneous emission of the emitter can be enhanced or suppressed by the cavity modes, while in strong coupling regime, vacuum Rabi splitting and photon blockade appear through periodically exchanging energy between the emitter and cavity photons (4, 5). Recently, through reducing the optical mode volume into micro/nano scale, the CQED has achieved great success in photonic crystals (6, 7), plasmonic nanocavities (8–11), whispering guided resonators (12), and various hybrid photonic systems (13–16), which paves a way to nanolaser, on-chip quantum devices, and scalable quantum networks (17).

Besides the ultrasmall mode volume, transversely confined light in the photonic structures induces the local spin of light, whose handedness has a one-to-one relation with respect to the propagation direction of the optical field enforced by time-reversal symmetry (18–21). If one puts a circularly polarized emitter in these structures, the propagation direction of the emitted photons will be locked by the handedness of local spin, so-called the chiral photon-emitter coupling (22, 23). Hence, the propagation isolation of photons is able to avoid the signal disturbance and improve transmission efficiency, which can be utilized in some nonreciprocal quantum information components, e.g., chiral entanglement (24, 25), quantum gates (26, 27), switchings (28), isolators (29), and circulators (30).

However, in the coupling between the circularly polarized emitter and photons, to simultaneously realize the strong interaction of photon-emitter and propagation direction lock of photons, which will bring novel applications in nonreciprocal quantum devices, has not been reported yet. Here, by combining the advantages of the CQED and chiral coupling, we pro-

pose the coupled structure consisting of W1 PC and Ag nanoparticle (AgNP) (Fig. 1A), where high quality nanocavities are formed to guarantee an achievement of both weak and strong couplings. Through strong local field with high helicity in nanocavities, coupling strength of photon-emitter can be greatly enhanced, accompanied by almost unidirectional propagation of emitted photons. In weak coupling regime, total decay rate reaches over $4500\gamma_0$ (γ_0 is the spontaneous emission rate in vacuum), among which the rate of photon emission into the PC waveguide is $148\gamma_0$, which is one order larger than that with only W1 PC (19, 31). While for the strong coupling, by using a low loss band-edge mode, the linewidth of fluorescence spectra of Rabi splitting is about one-tenth of that with only the AgNP. For both cases, $\sim 95\%$ photons propagate unidirectionally. Moreover, though the mode design, the coupled structure is capable of routing different wavelength photons into opposite propagation directions. So this work bridges the fields between the CQED and the chiral coupling in photonic structures.

The electric field in the waveguide of W1 PC has non-zero spin (measured by helicity) to support single directional propagation of photons with high coupling efficiency (32–34), but its intensity is generally very low in the position with high helicity (Fig. S1, D and E) (26). So it is difficult to arrive the strengthened photon-emitter coupling, for example, the decay rate of circularly polarized emitter in the W1 PC is only 10 times of γ_0 (19). To overcome this problem, the AgNP, which has achieved success in the Purcell enhancement and vacuum Rabi splitting due to the ultrasmall mode volume (8–10), is used as a nanocavity to enhance the interaction here. Furthermore, only depending on the individual nanoparticle structure, the propagation direction lock of photons can not be attained due to the lack of guided channel. So combining the advantages of two structures, i.e., the high local helicity in the waveguide of PC and the strong localized field of the AgNP, we propose the coupled structure of W1 PC and AgNP to demonstrate a strengthened photon-emitter coupling with unidirectional photon propagation.

After the mode hybridization of the PC and AgNP, three optical modes arise, i.e., modes

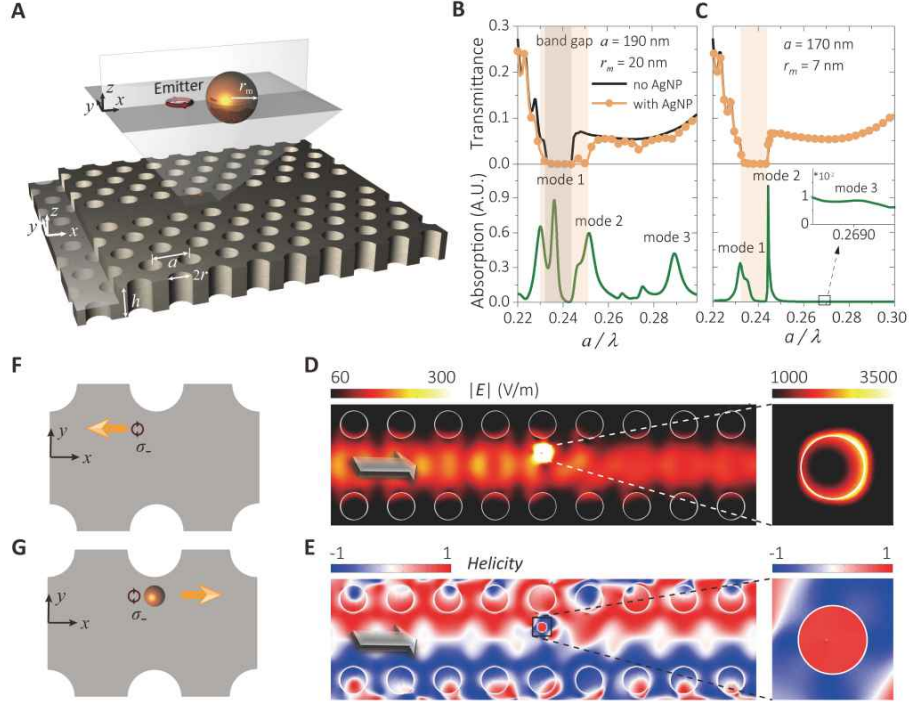


Figure 1: Optical modes of coupled W1 PC and AgNP structure. (A) Schematic diagram of coupled system with $h = 0.84a$ and $r = 0.29a$. Transmittance spectra of PC and the absorption spectra of the AgNP embedded in the center layer of PC for (B) $a = 190$ nm and $r_m = 20$ nm and (C) $a = 170$ nm and $r_m = 7$ nm. The center of AgNP is located at the xy -plane with $y = 50$ nm. Compared (B) with (C), large AgNP leads to the widening of the photonic band gap. Modes 1 and 3 are the dipolar and quadrupolar modes of the AgNP in the PC, while mode 2 of the AgNP raising at the band edge of the PC is induced by their hybridization. (D) The electric field and (E) its helicity distributions of xy -plane in the PC with the existence of the AgNP, where the arrows depict the propagation direction of the light. The insets show the details near the AgNP within the area of 80 nm \times 80 nm. (F) Left and (G) right propagation of emitted photons from the σ_- emitter without and with the AgNP along the waveguide of PC. Opposite propagation direction comes from the coupling of spin and orbit angular momentum.

1 and 3 are the dipolar and quadrupolar modes of AgNP, and mode 2 is the band edge mode appearing at the edge of photonic band (Fig. 1, B and C). Here W1 PC is chosen with the thickness $h = 0.84a$, the hole radius $r = 0.29a$, and refractive index $n = 3.45$, where a is the lattice constant, and the computations are performed by the commercial COMSOL Multiphysics and FDTD softwares (Fig. S1, B and C). When the radius r_m of AgNP is 20 nm and $a = 190$ nm, there is a widening of band gap of PC due to a strong mode coupling between two structures (Fig. 1B). In contrast, for $r_m = 7$ nm and $a = 170$ nm, the size of AgNP is too small to affect the band of the PC (Fig. 1C). More details of mode coupling are shown in Fig. S2. After the parameter optimization, mode 3 in Fig. 1B, which is situated at the guided band of the PC, acts as a nanocavity to provide large Purcell enhancement and effective guidance of photons. While mode 2 in Fig. 1C is suitable to realize strong coupling owing to its extremely narrow linewidth.

The emitted photons in chiral photon-emitter coupling have an propagation direction lock along the waveguide of the PC depending on the handedness of local spin where the emitter is. If without the AgNP, the electric field in the PC has a symmetrical distribution, while its helicity (the helicity of z direction is defined as $\frac{2\text{Im}[E_x E_y^*]}{|E_x|^2 + |E_y|^2}$ (35)) distribution is anti-symmetrical (Fig. S1E) (32). If we put a σ_- emitter into the upside of the channel, the emitted photons will excite the guided mode with right-handed spin and will be locked to the left direction (Fig. 1F). Then, consider the hybrid PC and AgNP system. If we take the mode 3 in Fig. 1B as an example, the electric field and its helicity distributions in the waveguide of the PC are almost the same as those without the AgNP (Fig. 1, D and E) except the region around the AgNP. Namely, around the AgNP, there is a very strong local field (the inset of Fig. 1D) and its local helicity (the inset of Fig. 1E) has an opposite sign with that without the AgNP (Fig. S4). According to the same principle, if one puts a σ_- emitter into the near field region of AgNP, the emitted photons will spread to the right direction (Fig. 1G).

Then, Purcell enhancement of chiral coupling at the nanoscale is demonstrated. A σ_- emit-

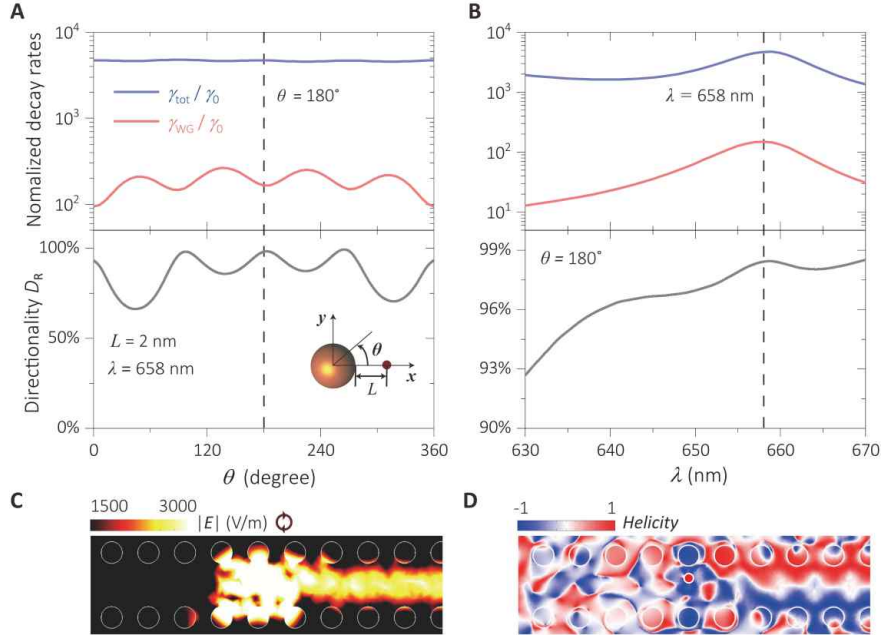


Figure 2: **Nanoscale Purcell enhancement and unidirectional propagation with chiral coupling.** Normalized decay rates $\gamma_{\text{tot}}/\gamma_0$ and $\gamma_{\text{WG}}/\gamma_0$ and the directionality D_R as a function of (A) θ and (B) λ . Here we use the quadrupolar mode of the AgNP (mode 3 in Fig. 1B) with the resonance wavelength of $\lambda = 658 \text{ nm}$ to realize the chiral coupling, and $a = 190 \text{ nm}$, $r_m = 20 \text{ nm}$, and $L = 2 \text{ nm}$. In (A), the maxima of $\gamma_{\text{WG}}/\gamma_0$ generally correspond to the minima of D_R and vice versa, while $\gamma_{\text{tot}}/\gamma_0$ keeps in a high range of 4600~4800. In order to balance the Purcell enhancement and the directional propagation, $\theta = 180^\circ$ is chosen in (B), where $\gamma_{\text{tot}}/\gamma_0 = 4700$ and $\gamma_{\text{WG}}/\gamma_0 = 148$, and 98.4% of guided part propagates along one direction due to the SOC. The distributions of (C) the electric field and (D) its helicity when a σ_- emitter excites the quadrupolar mode of the AgNP.

ter is put into the near field region of the resonant AgNP (mode 3 in Fig. 1B) with the distance of $L = 2$ nm. When it circles around the AgNP in the xy plane, i.e. θ is changed from 0° to 360° , Purcell factor (here the normalized total decay rate $\gamma_{\text{tot}}/\gamma_0$) remains very high values of $4500 \sim 4800$ (Fig. 2A), among which the guided part $\gamma_{\text{WG}}/\gamma_0$ is $95 \sim 264$ with the extreme values corresponding to the electric field maxima of the AgNP (the inset of Fig. 1D). It is noted that the guided part $\gamma_{\text{WG}}/\gamma_0$ alone is one order larger than the $\gamma_{\text{tot}}/\gamma_0$ (~ 10) of single W1 PC (Fig. S5). There is also a correspondence between the maximum of directionality D_R and the minimum of decay rates, where $D_{R/L} = \frac{W_{R/L}}{W_R+W_L}$ and $W_{R/L}$ is the energy power from the emitter into the right or left end of the channel (Fig. S6). This correspondence can be explained as follows. If the σ_- emitter is placed at the positions with the higher helicity, more emitted photons couple to the eigenstate mode with the same spin, leading to the maxima in D_R curve. In contrast, if the emitter is located at the lower helicity region, such as for $\theta = 45^\circ$, the directionality D_R is small, but two channels (to left and right directions) can transmit more photons (Fig. S9), so the maxima of $\gamma_{\text{WG}}/\gamma_0$ appear. By comparing these curves with the insets of Fig. 1, D and E, it is proved that strong local field leads to a large Purcell enhancement and high helicity results in a good directionality.

To balance the inconsistency between the decay rate and directionality, in Fig. 2B, the parameter of $\theta = 180^\circ$ is chosen. At the resonance wavelength of $\lambda = 658$ nm, both the Purcell enhancement in guided part and the directionality reach the highest values. Especially, in the spectral range of 655 nm \sim 661 nm, $\gamma_{\text{tot}}/\gamma_0$ and $\gamma_{\text{WG}}/\gamma_0$ can reach 4200 and 110 as well as 98% of the guided photons propagates unidirectionally. Fig. 2, C and D depicts the electric field and local helicity distributions when the electromagnetic mode is excited by the σ_- emitter with $\lambda = 658$ nm. As mentioned above, the existence of the AgNP changes the local helicity of the nanoarea where the emitter is. So the propagation direction is opposite to that if without a AgNP. Moreover, if now we put a σ_+ emitter near the AgNP, the photons will be launched to

the opposite direction according to the symmetry (Fig. S10).

Furthermore, the coupled structure is also capable of separating the different wavelength photons into opposite propagation directions. For example, in present coupled system, if the AgNP is substituted by a silver nanoblock with the length of 25 nm and the height of 10 nm, its optical modes appear at the wavelength of 706 nm and 639 nm respectively (Fig. S11A). As shown in Fig. S11, E and F, if putting a σ_- emitter with $\lambda = 706$ nm at the corner of the block, the guided part of emitted photons with $\gamma_{\text{WG}}/\gamma_0 = 389$ is steered to the left direction with the directionality of $D_L = 73\%$, while for the emitter with $\lambda = 639$ nm, the guided photons with $\gamma_{\text{WG}}/\gamma_0 = 76$ are selected to the right directions with $D_R = 89\%$ (Fig. S11, B and G). The reason is that, for different resonant wavelengths, the local helicity at the corner of the block has the opposite sign, i.e., more than zero or less than zero (Fig. S11, C and D). So the photons with the same spin will propagate to different directions, which may be used in on-chip routing single photons source.

Next, the vacuum Rabi splitting of energy levels in the chiral coupling is demonstrated. We put the AgNP near the waveguide of the PC (inset of Fig. 3A) and demonstrate that the appearance of the band-edge mode is independent of the position of the AgNP (Fig. S12). In Fig. 3A, the mode (mode 2 in Fig. 1C) appearing at the edge of photonic band with $\lambda = 695.7$ nm has a very narrow linewidth of $\kappa = 3.1$ meV, which is only one-tenth of the dipole mode of an AgNP in homogenous medium (Fig. S3). So for $\lambda = 695.7$ nm, $\Delta\lambda = 1.2$ nm and its quality factor Q is 580. Corresponding to the mode excitation, there is an electric field enhancement inside the waveguide of the PC, but the local field around the AgNP is two orders stronger than that surrounding it in the waveguide (Fig. 3B). Then, taking $\theta = 40^\circ$ and $\theta = 257^\circ$ as examples, with varying the distance L , coupling coefficients g between a σ_- emitter with the dipole moment $\mu = 0.2$ enm and the nanocavity are shown in Fig. 3D. For both cases, g decreases exponentially as an increment of L . Especially, for $L = 2$ nm and $\theta = 257^\circ$, $g = 4.28$

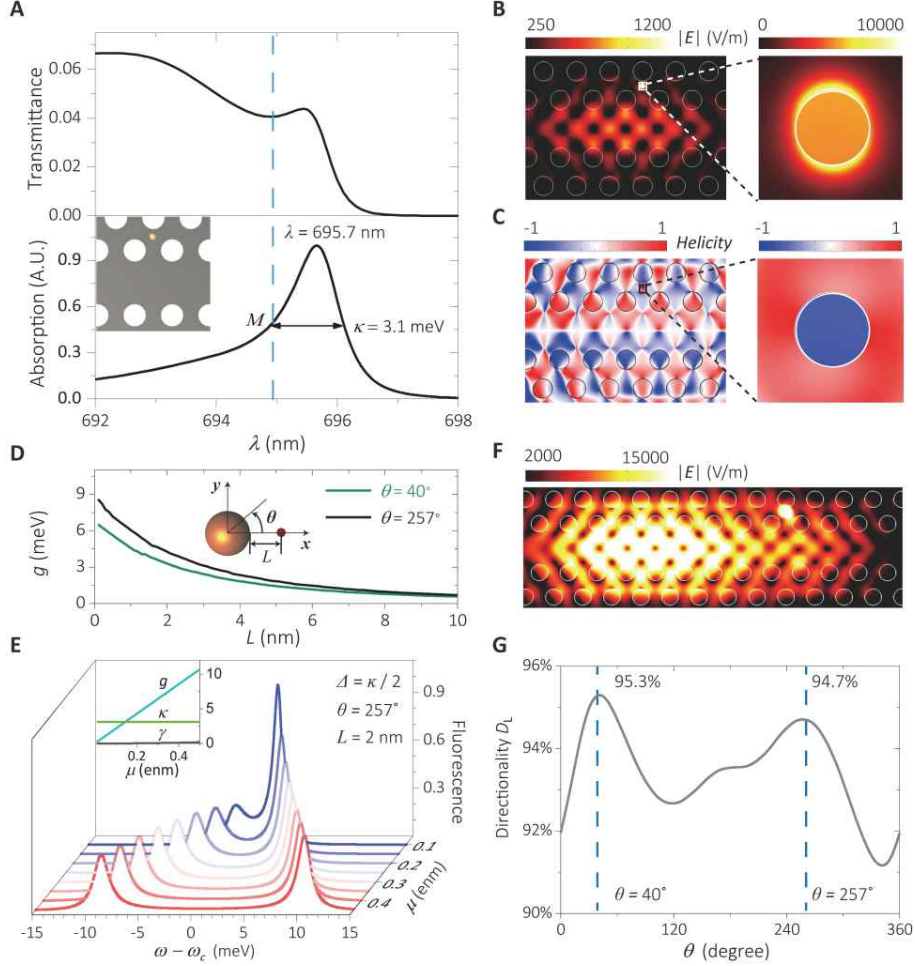


Figure 3: Rabi splitting of fluorescence spectra and uni-directional propagation with chiral coupling. (A) Transmittance spectra of PC and absorption spectra of the AgNP of the band edge mode (mode 2 in Fig. 1C). Here $a = 170$ nm and $r_m = 7$ nm. The mode at $\lambda = 695.7$ nm, raised by the mode hybridization of PC and AgNP, has a very narrow linewidth of $\kappa = 3.1$ meV. (B) The electric field and (C) its helicity distributions of the band edge mode with the insets of the region of 30 nm \times 30 nm. (D) Coupling coefficient g between the σ_- emitter and photon with varying the distance L for $\theta = 40^\circ$ and $\theta = 257^\circ$. (E) Fluorescence spectra of the quantum emitter as a function of $\omega - \omega_c$ with varying dipole moment μ . Here $\omega_c = 2\pi c/\lambda$. The inset shows the parameters g , γ , κ in dependence on μ . The asymmetry of fluorescence spectra comes from the nonzero detuning Δ between the emitter and the nanocavity. (F) The electric field distribution for $\theta = 257^\circ$ when a σ_- emitter excites the band edge mode. (G) Directionality D_L of guided photons with varying θ . In (E) to (G), the detuning $\Delta = \kappa/2$.

meV, $\kappa = 3.1$ meV, and the decay rate $\gamma = 0.03$ meV. Thereby, the strong coupling condition $g > (\kappa, \gamma)$ can be easily satisfied (36).

By using the Python toolbox, the fluorescence spectra of a σ_- emitter coupled with the band edge mode are obtained. Considering that the directionality D_L at $\theta = 257^\circ$ is 94.7% (Fig. 3G) and the point M with the frequency detuning $\Delta = \kappa/2$ (between the emitter and cavity mode) is within the guided band of the PC which is benefit to the photons transmittance (Fig. 3A), we choose the parameters of $\theta = 257^\circ$, $L = 2$ nm, and $\Delta = \kappa/2$. It is found that the Rabi splitting in fluorescence spectra starts to appear at $\mu = 0.1$ enm and becomes larger with its increment; while for $\mu = 0.2$ enm, there is an apparent energy exchange between the emitter and cavity photons (Fig. 3E). Besides, owing to the existence of detuning Δ , the symmetry of fluorescence spectra is broken. The energy splitting and the spectral linewidth are roughly coincident with $\sqrt{4g^2 + \Delta^2 - \frac{(\kappa-\gamma)^2}{4}}$ and $\frac{\kappa+\gamma}{2}$ of the dressed state theory (36, 37). The linewidth of fluorescence spectra is about one-tenth of that if only the existence of the AgNP. Hence, superior to the properties of individual AgNP, the narrower linewidth of the band edge mode leads to the earlier appearance of Rabi splitting with the smaller μ .

In this case, the sign of electric field helicity around the AgNP (the inset of Fig. 3C) is opposite to that in Fig. 1E and Fig. 2D. So if now putting a σ_- emitter into its near field region, we can see that the photons will propagate in opposite direction (Fig. 3F), i.e., along $-x$ direction. Compared with the case of $\Delta = 0$ (Fig. S13), more photons can be transmitted because at the point M the frequency of emitted photons lies in the guided band of the PC. For $L = 2$ nm and $\Delta = \kappa/2$, if letting the emitter walk a circle around the AgNP, the directionality D_L reaches its maximum at $\theta = 40^\circ$ and 257° . Corresponding to these maxima, $\sim 95\%$ of guided photons propagates into one direction along the waveguide of the PC, which may be used in the nonreciprocal quantum nanophotonic devices (23).

Finally, we address the fabrication possibility of our scheme. Nowadays, single AgNP (8)

and PC (34) can be fabricated by state-of-the-art nanotechnology. Besides, single emitters embedded in photonic-crystal waveguide in the experiments have also been realized through scanning tunneling microscopy (31). The main challenge to realize efficient chiral coupling is how to control the relative positions between the emitter and the AgNP precisely. This problem may be solved by using an atomic force microscopy tip to move the AgNP after the position of an emitter is fixed (38). To obtain circularly polarized photons with different frequency, first two circularly polarized states $|+\rangle$ and $|-\rangle$ of the atoms (39) or quantum dots (26) are generated by applying a strong magnetic field in z direction; then, by selecting the frequency of the excitation laser, the emitters only emit σ_- or σ_+ photons. Thus, it may be possible to achieve our scheme in experiment in near future.

In summary, we have established a photonic interface of chiral CQED by proposing the coupled photonic crystal and plasmon nanoparticle structure. We clearly state that the key element of chiral CQED is the joint action of strong local field and its high helicity, which provides a strengthened light-emitter coupling with good directionality of emitted photons. Using the basic idea presented here, other kinds of combined photonic structures could be designed, such as the coupled nanowire and nanoparticle, photonic crystal and nanocavity systems, and so on. The results bridge the fields of the CQED and the chiral coupling, which greatly enriches the contents of light-emitter interaction at the nanoscale. By combining the advantages of these two fields, we provide a possible platform for on-chip nonreciprocal quantum light sources, quantum circuits, and scalable quantum network.

Acknowledgement

We thank X. Hu and Y. Ao for helpful discussions. This work is supported by the National Key R&D Program of China under Grant No. 2018YFB1107200, and by the National Natural Science Foundation of China under Grants No. 11525414 and No. 11734001.

Material and Methods

1. Computation module

We use the commercial COMSOL multiphysics software to perform the simulations. The TE-like PC, containing 11×12 unit cells shown in Fig. S1A, is placed in the middle of a three-dimensional module with the height of $h + 1 \mu\text{m}$ (Fig. S1B). To minimize boundary reflections and form an infinite space, scattering boundary condition is used to surround the module. An AgNP, whose permittivity is taken from the experimental data (40), is embedded in the middle plane of the waveguide of PC. By incidenting a beam of plane wave propagating along the x -axis, or putting an oscillating point dipole inside the PC, modes of the coupled PC and AgNP structure can be excited.

The circular polarization of the light is represented by helicity, which is defined as (35)

$$C = \frac{|E_{\text{LCP}}|^2 - |E_{\text{RCP}}|^2}{|E_{\text{LCP}}|^2 + |E_{\text{RCP}}|^2}, \quad (1)$$

where $E_{\text{LCP/RCP}}$ is the left- or right-component of the electric field which is related to the basis. If we choose the basis of $\frac{\hat{x}+i\hat{y}}{\sqrt{2}}$, $\frac{\hat{x}-i\hat{y}}{\sqrt{2}}$, and \hat{z} , the helicity in the z -direction can be written as $C(z) = \frac{2\text{Im}[E_x E_y^*]}{|E_x|^2 + |E_y|^2}$. In the same way, we can derive $C(x) = \frac{2\text{Im}[E_y E_z^*]}{|E_y|^2 + |E_z|^2}$ and $C(y) = \frac{2\text{Im}[E_z E_x^*]}{|E_z|^2 + |E_x|^2}$. From Eq. (1), $C = 1$ represents the left-polarized light and $C = -1$ is the right-polarized light. In the COMSOL module, the left- and right-handed polarized plane waves along z -axis are given as $\vec{E}_{\pm} = E_x \hat{x} + E_y \hat{y} = \frac{E_0 \hat{x} + E_0 e^{\mp \pi/2} \hat{y}}{\sqrt{2}}$, where E_0 is the amplitude of the electric field and E_y is $\pm \pi/2$ out of phase with E_x . Similarly, the left- and right-handed polarized emitters are set as oscillating point dipoles for $\sigma_{\pm} = \frac{\mu \hat{x} + \mu e^{\mp \pi/2} \hat{y}}{\sqrt{2}}$, where μ is the magnitude of the dipole moment. The transmittance spectra of the PC is defined as I_t/I_0 , where I_t and I_0 are the light intensity in the incident and exit surfaces of the PC. In this text, the light is incident on the left end of the PC and the right end is used as receiving surface to collect photons.

2. Photonic band diagram of photonic crystal

We compute the photonic band diagram of the PC by a finite-difference time-domain (FDTD) method with commercial software (Lumerical) (Fig. S1C). To reduce the computation process, a two-dimensional module, where the thickness of the PC is represented by a modified refractive index n_{eff} , is performed. Through boundary mode analysis in the COMSOL module, we obtain $n_{\text{eff}} = 2.95$. Compared with the transmittance spectra in Fig. 1, B and C, the band gap in Fig. S1C is coincident with that in the transmittance spectra obtained by COMSOL software.

3. Computation of the coupling coefficients

Three physical processes are included in the CQED systems: the coupling between the cavity photons and the emitter, the decay of the emitter, and the cavity loss, whose coefficients are labeled as g , γ , and κ , respectively. According to their relations, two typical regimes exist, i.e., weak coupling for $g \ll \gamma, \kappa$ and strong coupling for $g \gg \gamma, \kappa$ (3).

Weak coupling

In weak coupling regime, the emitter decays through three channels: guiding along the waveguide, radiating into far field and nonradiative loss. Thus the total decay rate γ_{tot} is equal to the sum of these decay rates, i.e., $\gamma_{\text{tot}} = \gamma_{\text{rad}} + \gamma_{\text{nr}} = \gamma_{\text{WG}} + \gamma_{\text{free}} + \gamma_{\text{nr}}$, where γ_{free} is the decay rate to the free space. The total normalized decay rate can be obtained from $\gamma_{\text{tot}}/\gamma_0 = W_{\text{tot}}/W_0$ (43), where W_{tot} and W_0 are the total emitted energy power of an emitter in the coupled system and in vacuum, respectively. The energy power of the emitter in the COMSOL module is given by the surface integration of a nanosphere containing the emitter over the energy flows, which can be expressed by $W_{\text{tot}} = \int \int_{\Sigma} \vec{S} \cdot d\Sigma$ and \vec{S} is the Poynting vector on the nanosphere (15). Similarly, the guided part along the waveguide is calculated by $\gamma_{\text{WG}}/\gamma_0 = W_{\text{WG}}/W_0$, where W_{WG} is the energy power in the receiving surfaces—right and left surfaces of the module.

Strong coupling

The dynamics of an emitter-nanocavity coupled system in strong coupling regime can be represented by JC-model, where the Hamiltonian and dynamical equation are given by

$$H = \omega_e \sigma^+ \sigma + \omega_c a^+ a + g(\sigma^+ a + a^+ \sigma), \quad (2)$$

and

$$\dot{\rho} = i[\rho, H]/\hbar + \frac{\gamma}{2}(2\sigma\rho\sigma^+ - \{\sigma^+\sigma, \rho\}) + \frac{\kappa}{2}(2a\rho a^+ - \{a^+a, \rho\}), \quad (3)$$

where ω_e and ω_c are the frequencies of the emitter and the nanocavity, σ (σ^+) is lowering (raising) operator of the emitter and a (a^+) is bosonic annihilation (creation) operator of the AgNP, respectively. The physical process in this system is that the emitter and the nanocavity exchange energy with coupling coefficient g , and simultaneously, photons also lose because of the atomic decay and Ohmic loss of the cavity, with coefficients labeled as γ and κ . In the following we show how to compute these coefficients in the COMSOL software.

a. Coupling coefficient g

The AgNP is excited by the light propagating along the waveguide of the PC or by the background electric field (the case for the AgNP in the homogeneous medium). Following the equations and method in Refs. (16, 41), $\hbar g = \mu E_s$ where E_s is the electric field of AgNP corresponding to a single excitation and can be written as

$$E_s = \tilde{E} / \sqrt{\frac{W}{\hbar\omega_c}}, \quad (4)$$

where \tilde{E} is the excited electric field of the nanocavity, $\sqrt{\frac{W}{\hbar\omega_c}}$ symbols the number of photons with energy of $\hbar\omega_c$, and W is the total energy of the cavity mode which is calculated by energy density integration in the whole space (16):

$$W = \frac{1}{2} \int \frac{\partial}{\partial \omega} [\omega \text{Re}[\varepsilon(\omega)]]|_{\omega=\omega_c} |\tilde{E}|^2 dV + \frac{1}{2} \int \mu_0 |\tilde{H}|^2 dV. \quad (5)$$

b. Cavity loss κ

The cavity loss κ is the fullwidth at half-maximum (FWHM) of its extinction spectra, including the scattering and absorption of the cavity. Because the FWHM of scattering and absorption spectra are almost the same (42), κ is derived from the absorption spectrum here. In the COMSOL module, the mode of AgNP is excited by a nearby oscillating point dipole. By volume integrating the AgNP over the power density, the resistive loss W_{nr} is obtained. κ of the AgNP in the homogeneous environment with refractive $n = 3.45$ is shown in Fig. S3.

c. Decay rate γ

Decay rate γ here means that the atomic decay rate to the modes other than the cavity mode, i.e., except for the nonradiative decay caused by the loss of the AgNP. Therefore, γ is equal to the total decay rate minus the nonradiative part, i.e., $\gamma = \gamma_{\text{tot}} - \gamma_{\text{nr}}$, which can be obtained by $\gamma = \frac{W_{\text{tot}} - W_{\text{nr}}}{W_0} \gamma_0$ with $\gamma_0 = \omega^3 \mu^2 / 3\pi \epsilon_0 \hbar c^3$ (44).

4. Fluorescence spectra of the quantum emitter

Python toolbox is performed to derive the resonance fluorescence spectrum of the CQED system by Fourier transformation electric intensity $\langle E^-(\vec{r}, t) E^+(\vec{r}, t) \rangle$, with the expression of $S(\vec{r}, \omega_0) = \frac{1}{\pi} \text{Re} \int d\tau \langle E^-(\vec{r}, t) E^+(\vec{r}, t) \rangle e^{i\omega_0 t}$ (44, 45). By increasing the dipole moment of the emitter, Rabi splitting appears in the fluorescence spectra (Fig. 3E and Fig. S13). When the transition frequency of the emitter is coincident with the resonant frequency of the nanocavity, the peaks of Rabi splitting are symmetry (Fig. S13). By contrast, asymmetry occurs as the emitter frequency deviates from that of the AgNP mode (Fig. 3E).

Supplementary Text

1. The electric field and its helicity for the modes of the AgNP

In the following, we analyse the electric field and its helicity for the mode of the AgNP in a homogeneous medium with the refractive index of $n = 3.45$. Figure S4, A-B, and C-D depicts the electric field and helicity distributions of the AgNP in the xy - and yz -plane, respectively. An AgNP with the radius of 7 nm is excited by a right-handed plane wave polarized in the xy -plane. The wavelength of the incident light is 625 nm, corresponding to the wavelength of the dipole mode. It is seen that the electric field in the yz -plane is similar to that of a linearly polarized dipole in the y direction. While in the xy -plane, the absolute value of the electric field is almost homogeneous surrounding the AgNP. To be mentioned, the helicity around the AgNP in the xy plane has an opposite sign against that of the excited light. This phenomenon can be explained as follows. The equivalent dipole moment of the AgNP excited by a plane wave with $\vec{E} = [1, i, 0]E_0e^{-i(k_z z - \omega t)}$ is given as

$$\vec{p}_{\text{MNP}} = 4\pi\epsilon_b\epsilon_0r_m^3\Gamma(E_0\hat{x} + iE_0\hat{y}), \quad (6)$$

where $\Gamma = (\epsilon_m - \epsilon_b)/(\epsilon_m + \frac{n'+1}{n'}\epsilon_b)$ with the permittivity ϵ_m of the AgNP and ϵ_b of the host medium (46). Take the dipole mode as example, namely, $n' = 1$, $\Gamma = (\epsilon_m - \epsilon_b)/(\epsilon_m + 2\epsilon_b)$ and the resonant condition is $\epsilon_m = -2\epsilon_b$. Under the resonant condition, $[p_x, p_y] \propto [-i, 1]$, which has the same form with that of a σ_- emitter whose near field has > 0 helicity in the yz -plane. Similarly, the local polarization of the higher-order modes of the AgNP also has the same sign as that of the dipole mode.

2. Optical mode coupling between the PC and the AgNP

The transmittance spectra of the PC and the absorption spectra of the AgNP with various radius r_m are shown in Fig. S2. The same as in Fig. 1, B and C, mode 1 and mode 3 correspond to

the dipole and quadrupole modes of the AgNP and mode 2 is a band-edge mode. Here, lattice constant a is changed to make the mode of the AgNP situating at different frequency regions of PC, i.e., guided and band gap regions. Take $r_m = 7$ nm for example. As a increases, the dipole mode of the AgNP moves from the band gap to the guided band of the PC. Comparing Fig. S2, A to C, it is seen that narrow and sharp band-edge modes appear when the dipole mode of the AgNP locates at the band gap of the PC (Fig. S2C).

The gray region depicts the band gap of the PC without the existence of the AgNP. It is seen that the band gap is broadened as the radius r_m of the AgNP enlarges. Red shift of mode 1 and mode 3 in the absorption spectra is also clearly shown as an increment of r_m .

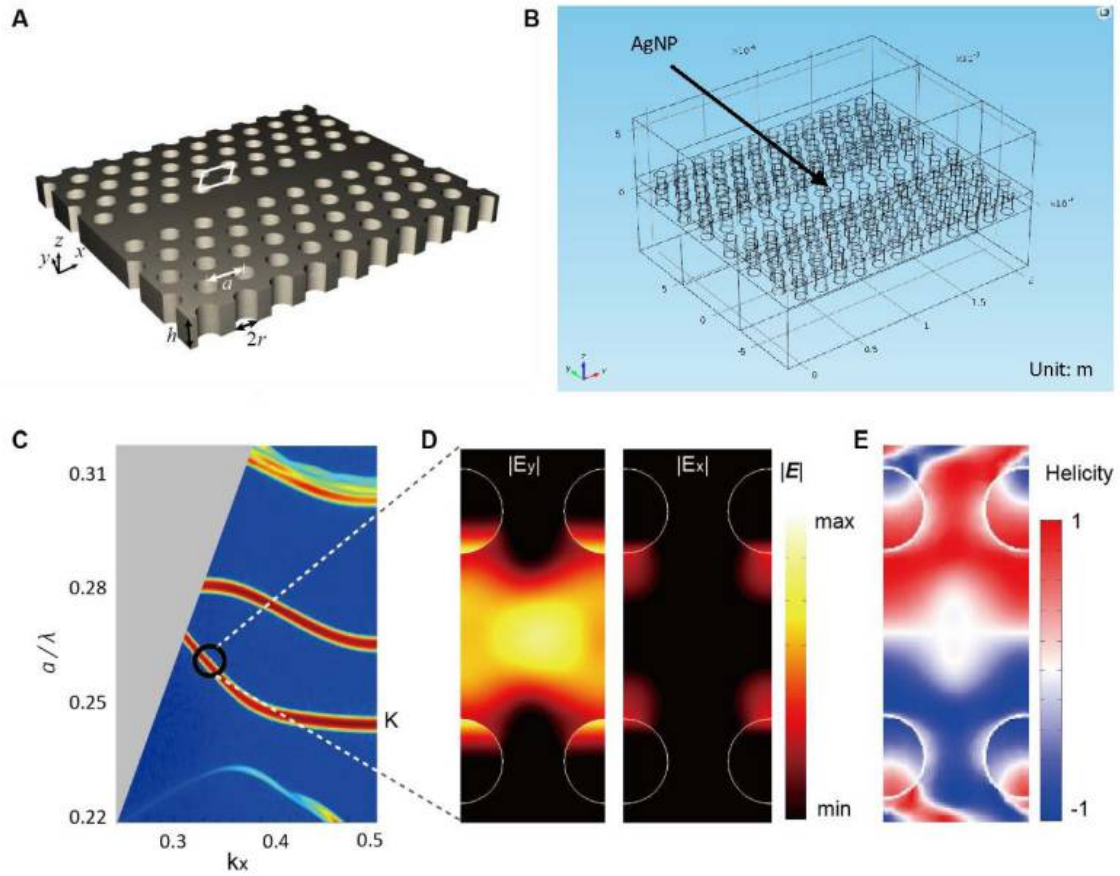


Figure S1: (A) Schematic diagram of the W1 PC and (B) computation module of COMSOL software. One unit cell of the PC is marked within the white lines in (A). (C) Photonic band diagram of the coupled W1 PC and AgNP structure for the period of $a = 190$ nm, the hole radius of $r = 0.29a$, the thickness of $d = 0.84a$, and the refractive index of $n = 3.45$. (D) The electric field components $|E_x|$ and $|E_y|$ and (E) helicity distributions of z direction when $a/\lambda = 0.26$. The electric field intensities are normalized by the maximum of $|E_y|$.

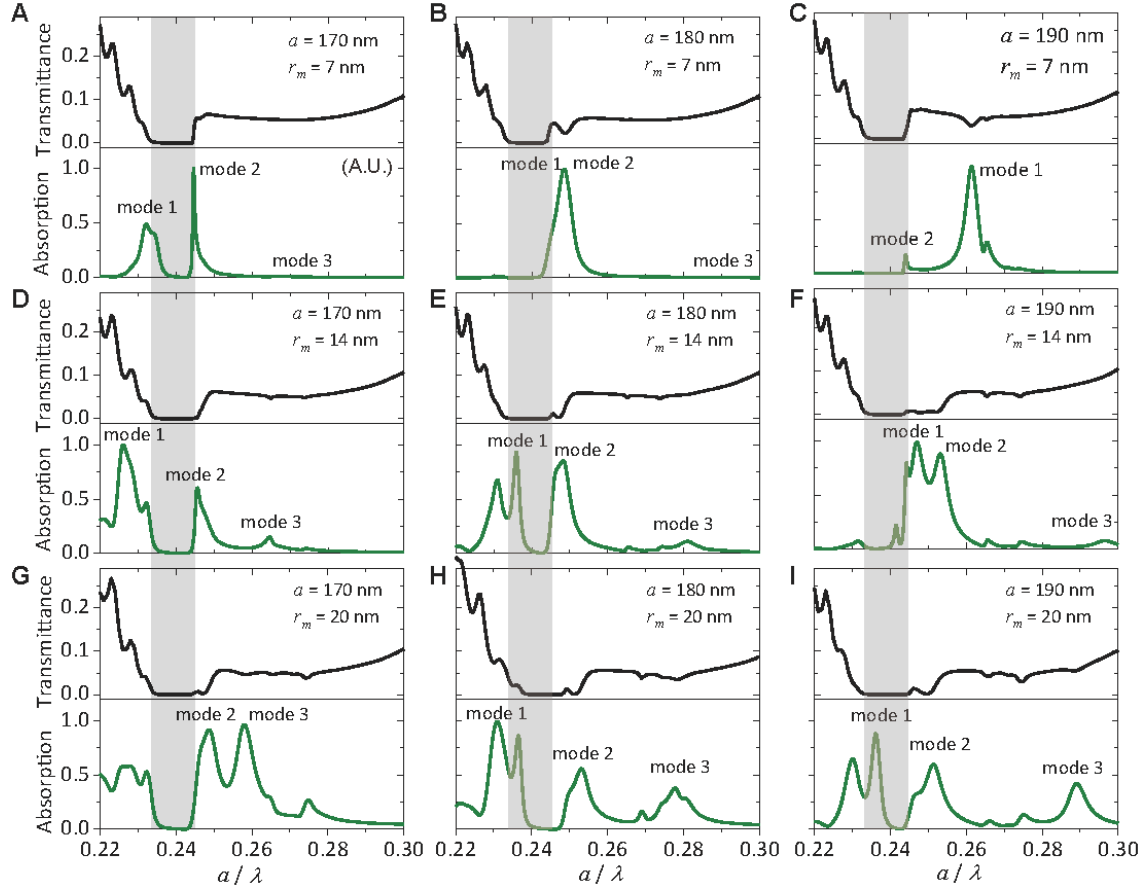


Figure S2: The transmittance spectra of the PC and the normalized absorption spectra of the AgNP with the radius of (A-C) $r_m = 7$ nm, (D-F) $r_m = 14$ nm, and (G-I) $r_m = 20$ nm. The parameters for $a = 170$ nm~ 190 nm are computed to change the coupling between the modes of the PC and AgNP. Fig. 1, B and C in the main text corresponds to (A) and (I), respectively, and the band gap of a PC without the AgNP is shown as the gray region. Mode 1 and mode 3 are the dipole and quadrupole modes of the AgNP and mode 2 is the band-edge mode corresponding to the K point in the band diagram of Fig. S1C. By increasing the radius of the AgNP, the band-edge mode always exists and its linewidth is increased. Specifically, when $a = 180$ nm and $r_m = 7$ nm, mode 1 is at the band edge of the PC so modes 1 and 2 are almost overlapped.

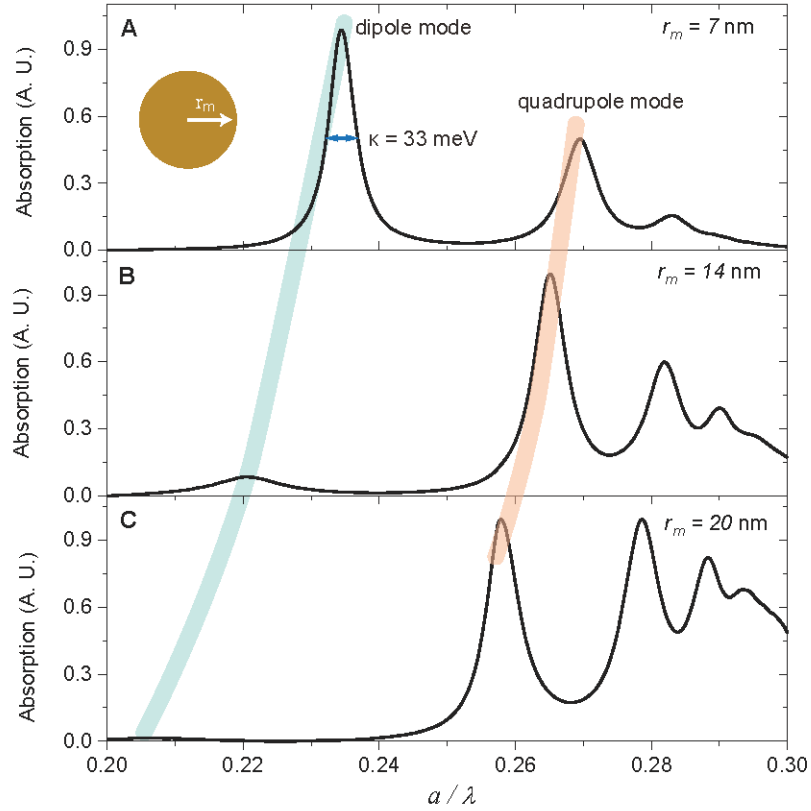


Figure S3: Absorption spectra of the AgNP in a homogeneous medium with refractive index of $n = 3.45$, for the radius of (A) $r_m = 7$ nm, (B) $r_m = 14$ nm, and (C) $r_m = 20$ nm, respectively. The wavelength is normalized by $a = 170$ nm to compare with the case of the AgNP embedded in the PC waveguide. For the AgNP with different size, red shift in the resonance wavelength occurs as r_m enlarges.

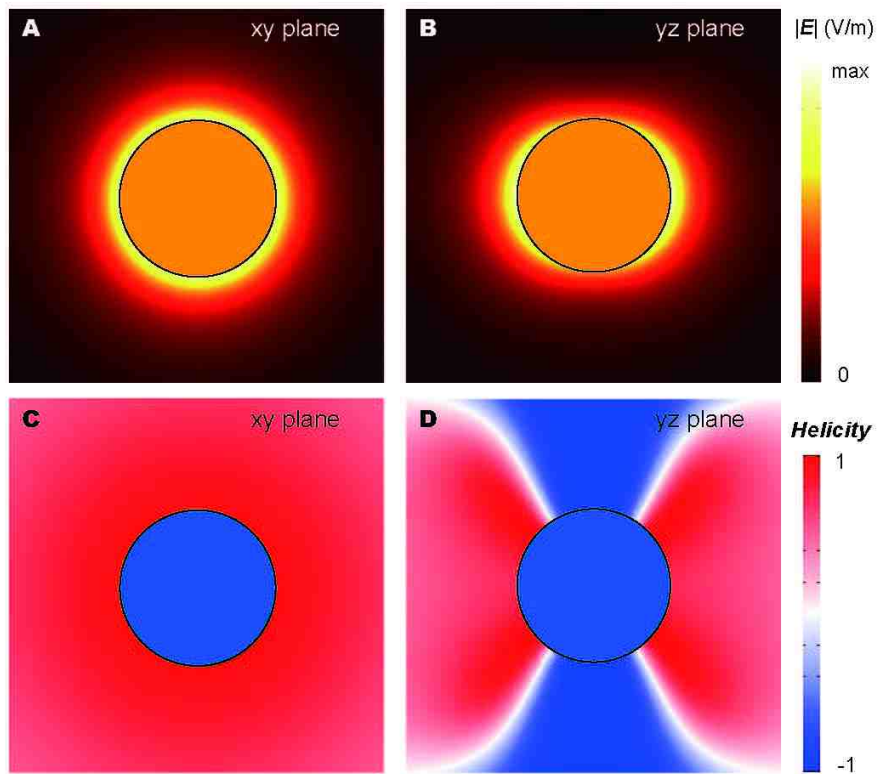


Figure S4: The electric field and helicity distributions of the dipole mode of an AgNP with $r_m = 7$ nm in the (A and C) xy and (B and D) yz planes embedded in a homogeneous medium with refractive index of $n = 3.45$. A right-handed polarized plane wave is used to excite the AgNP, which propagates along z direction. From (C), the helicity around the AgNP in the xy plane has an opposite sign against that of the excitation light.

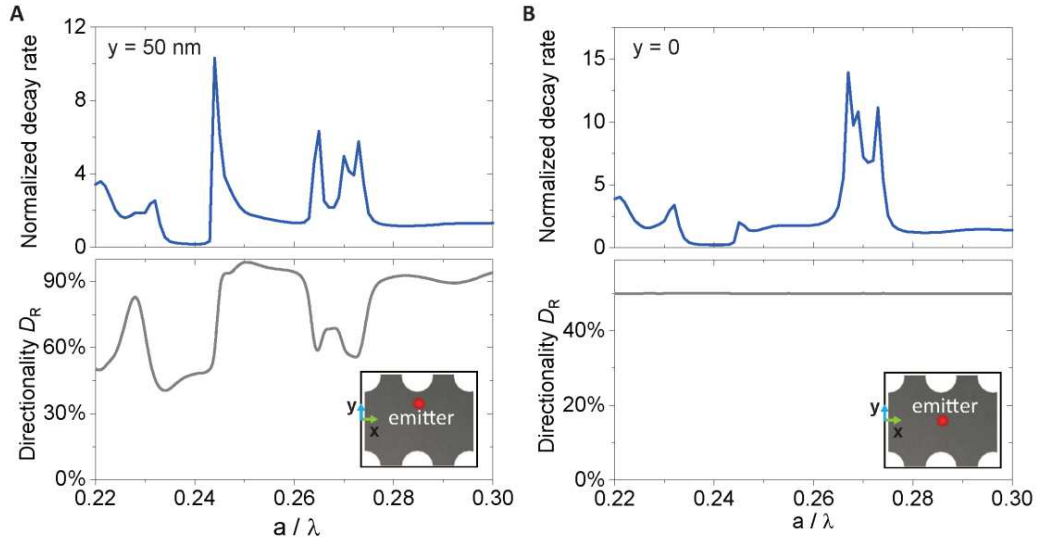


Figure S5: Total decay rates γ_{tot} normalized by γ_0 of a σ_- emitter embedded in the PC waveguide for (A) $y = 0$ and (B) $y = 50$ nm. $\gamma_{\text{tot}}/\gamma_0$ is almost less than 15 when a/λ is within the guided mode region (32). The directionality D_R for the emitter placed at (C) $y = 0$ and (D) $y = 50$ nm. The lattice constant is $a = 190$ nm.

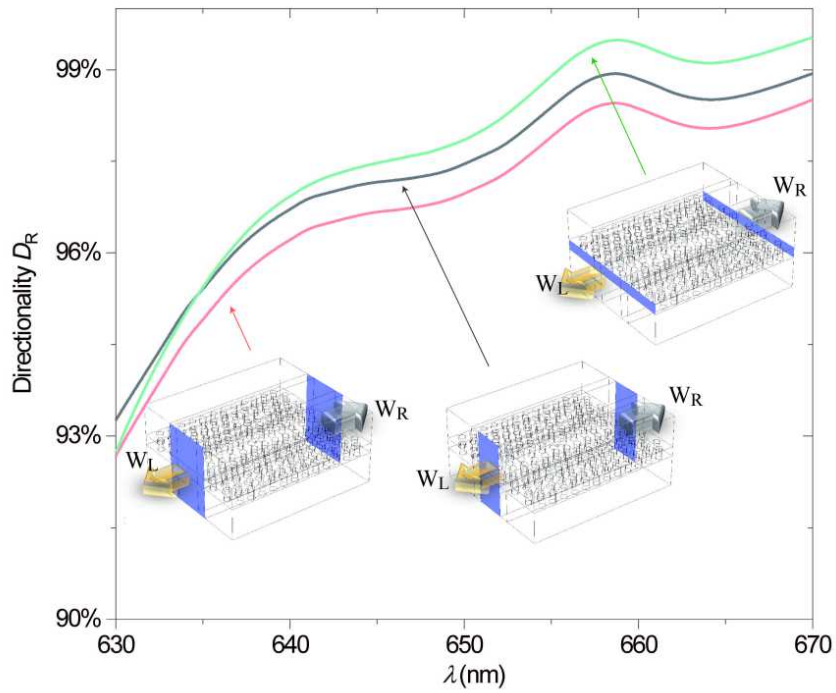


Figure S6: Directionality of the photons emitted from a σ_- emitter for different receiving surfaces to collect photons shown as the insets. Because the photons lose the lock of propagation direction in the free space, directionality D_R reduces a little when the surrounding environment is involved. However, the wavelength of the maxima in these three cases are not changed. Here, the emitter is set at $y = 50$ nm.

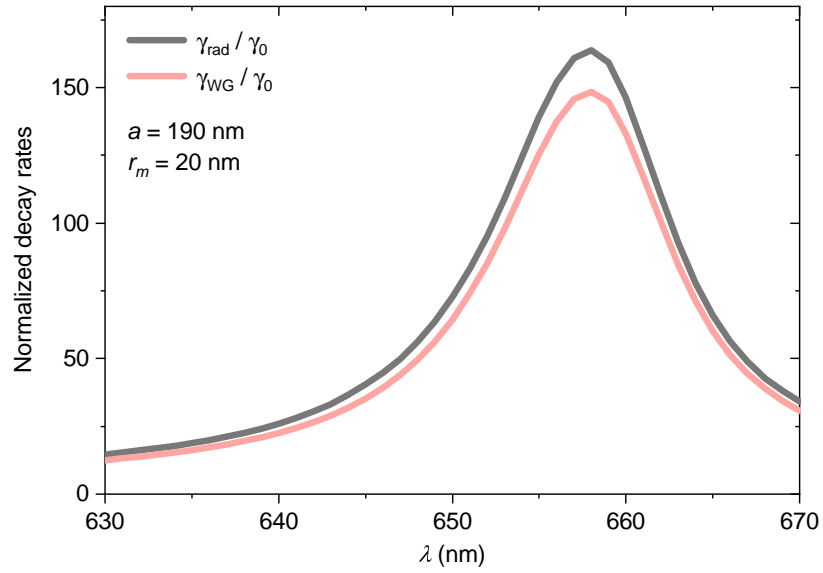


Figure S7: Normalized decay rates of the σ_- emitter in the coupled PC and AgNP structure for radiative part ($\gamma_{\text{rad}}/\gamma_0$) and along the waveguide ($\gamma_{\text{WG}}/\gamma_0$). More than 90% of the radiative photons is coupled to the waveguide of the PC.

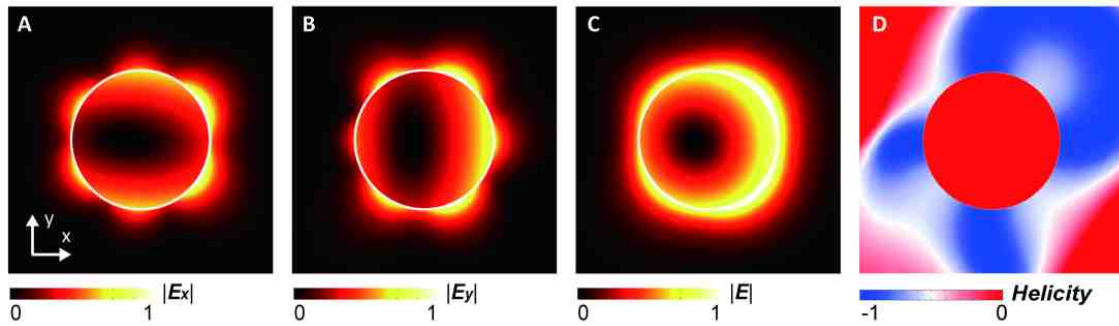


Figure S8: The electric field components (A) $|E_x|$ and (B) $|E_y|$, (C) the intensity of the total electric field $|E|$, and (D) the local helicity of z direction at the area of $80 \times 80 \text{ nm}^2$, corresponding to the mode 3 of Fig. 1B in the coupled PC and AgNP structure. The electric fields are normalized by the maximum of $|E|$. By changing the legend of helicity to $[-1, 0]$, the maxima and minima of helicity around the AgNP can be clearly recognized. The parameters are set as $a = 190 \text{ nm}$ and $r_m = 20 \text{ nm}$.

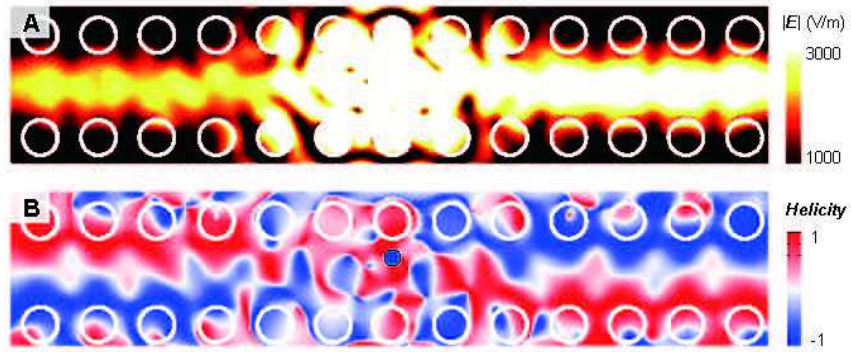


Figure S9: (A) Electric field and (B) its helicity of the σ_- emitter in the coupled PC and AgNP structure, for $r_m = 20$ nm, $y = 50$ nm, and $\theta = 45^\circ$. The photons propagate to two sides along the waveguide of PC, leading to small directionality D_R . The symmetry of helicity in both propagating channels is not broken compared with that at $\theta = 180^\circ$ in the main text.

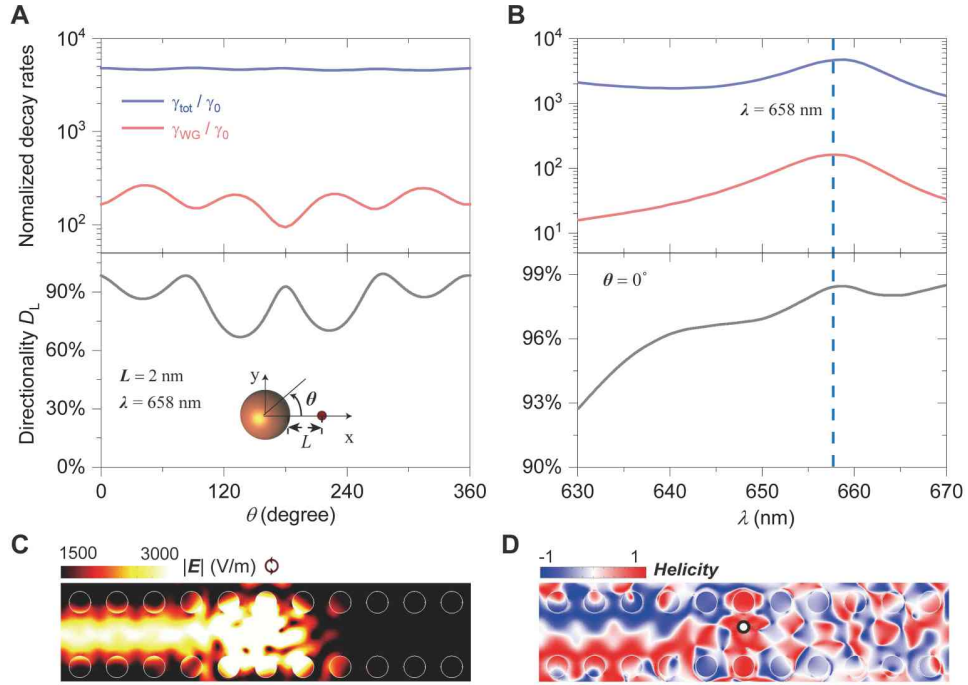


Figure S10: Normalized decay rates $\gamma_{\text{tot}}/\gamma_0$ and $\gamma_{\text{WG}}/\gamma_0$ of a σ_+ emitter and the directionality D_L of the emitted photons as a function of (A) θ and (B) λ for $a = 190 \text{ nm}$, $r_m = 20 \text{ nm}$, and $L = 2 \text{ nm}$. In (A), the maxima of $\gamma_{\text{WG}}/\gamma_0$ generally corresponds to minima of D_L and vice versa, while $\gamma_{\text{tot}}/\gamma_0$ keeps in a high range of $4600 \sim 4800$. $\theta = 0^\circ$ is chosen in (B). When $\lambda = 658 \text{ nm}$, Total Purcell enhancement reaches $\gamma_{\text{tot}}/\gamma_0 = 4700$ and $\gamma_{\text{WG}}/\gamma_0 = 148$, where 98.4% of emitted photons propagates to left direction. The distributions of (C) the electric field and (D) its helicity when a σ_+ emitter excites the quadrupolar mode of the AgNP. From the helicity distribution, the symmetry of the propagation is broken, whose direction is opposite to that of the σ_- emitter in Fig. 2D.

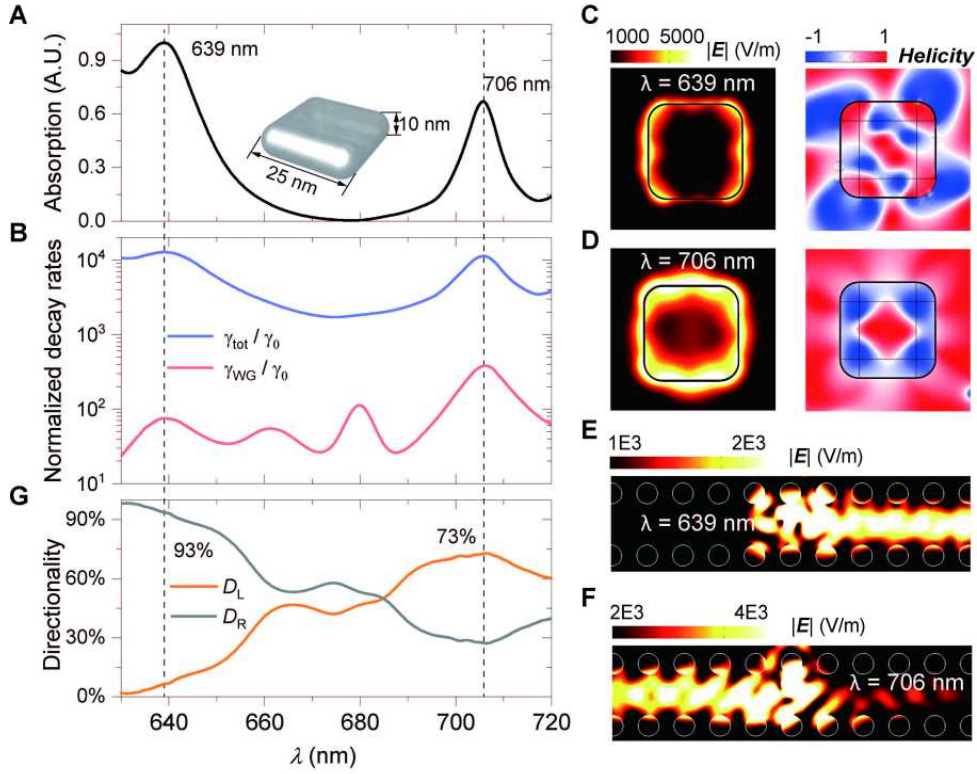


Figure S11: (A) Absorption spectra of a silver nano-block with the length of 25 nm and the height of 10 nm embedded in the waveguide of PC for $a = 180$ nm. Two adjacent resonance wavelengths of the block are 639 nm and 706 nm. (B) Normalized decay rate as a function of λ . Corresponding to two resonant wavelengths, $\gamma_{\text{tot}}/\gamma_0 = 12719$ and 11428 , and $\gamma_{\text{WG}}/\gamma_0 = 76$ and 389 , respectively. (C) The electric field and (D) helicity distributions for the nano-block in the resonance wavelengths, where the sign of helicity at the corner of the AgNP are opposite. By using this character of the helicity of the two modes, for $\lambda = 639$ nm, 93% of the photons emitted from σ_- emitter is guided to right direction and 73% to left direction for $\lambda = 706$ nm. The electric field (E) for $\lambda = 639$ nm and (F) for $\lambda = 706$ nm. (G) Directionality $D_{R/L}$ dependent on λ . Here, the nano-block is placed at $y = 50$ nm.

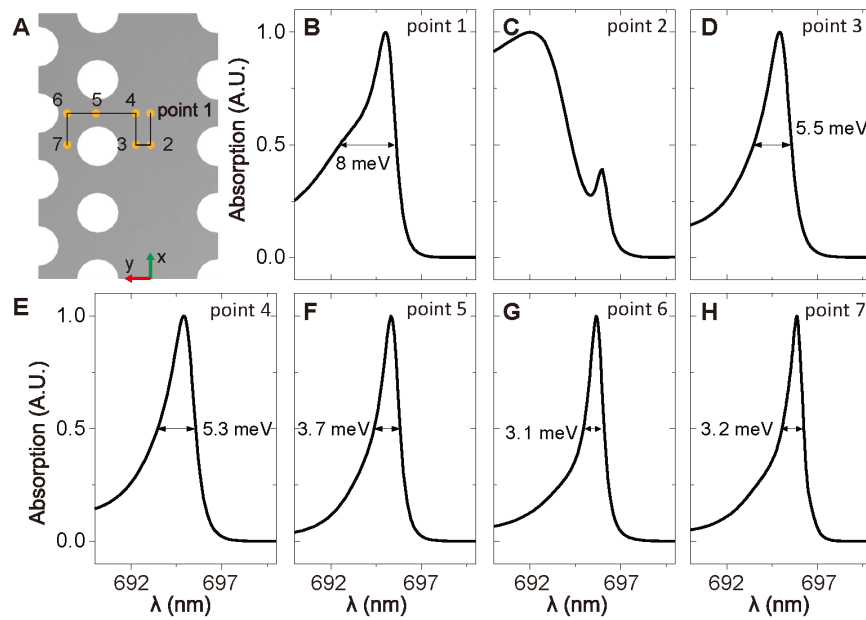


Figure S12: (A) Schematic diagram of the AgNP with $r_m = 7$ nm located in different positions of the PC. (B to H) The absorption spectra of the band-edge mode for various AgNP positions marked in (A). The linewidth κ of the AgNP is optimized by selecting its position. In the main text, point 6 with $\kappa = 3.1$ meV is used.

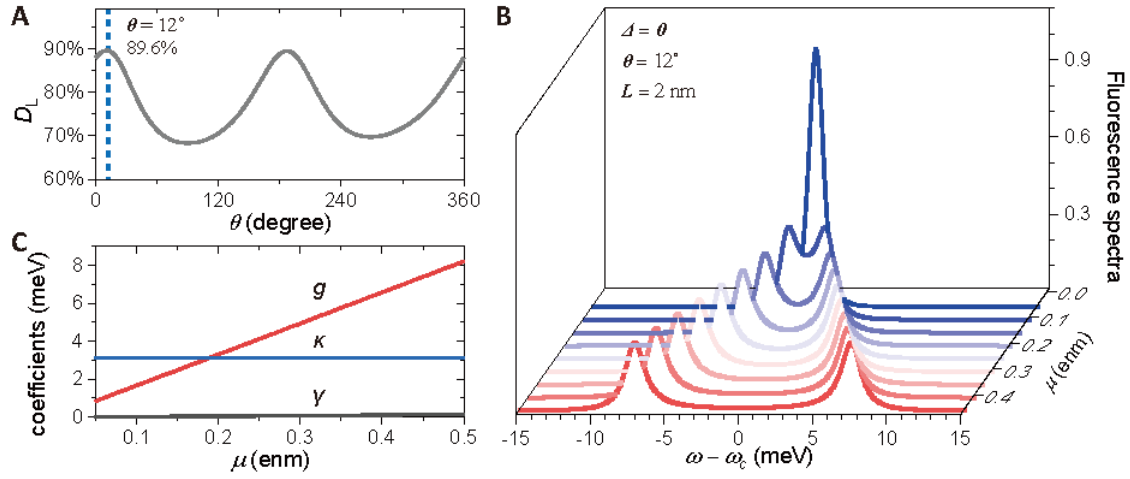


Figure S13: (A) Directionality D_L of emitted photons dependent on θ . The AgNP with $r_m = 7$ nm is placed at point 6 of Fig. S12. Directionality D_L reaches the maximum when $\theta = 12^\circ$ and 190° with the value of 89.6%. (B) Fluorescence spectra of the quantum emitter as a function of $\omega - \omega_c$ with varying dipole moment μ . The parameters g , γ , κ in dependence on μ are shown in (C). Here, $L = 2$ nm and the detuning Δ between the AgNP and emitter is zero.

References

1. S. Haroche, D. Kleppner, Cavity quantum electrodynamics. Phys. Today 42, 24-30 (1989).
2. R. Miller, T. E. Northup, K. M. Birnbaum, A. Boca, A. D. Boozer, H. J. Kimble, Trapped atoms in cavity QED: coupling quantized light and matter. J. Phys. B 38, S551-S565 (2005).
3. K. J. Vahala, Optical Microcavities. Nature 424, 839-846 (2005).
4. H. Walther, B. T. H. Varcoe, B.-G. Englert, T. Becker, Cavity quantum electrodynamics. Reports Prog. Phys. 69, 1325-1382 (2006).
5. H. J. Kimble, Strong Interactions of Single Atoms and Photons in Cavity QED. Phys. Scr. T76, 127-137 (1998).

6. T. Yoshie, A. Scherer, J. Hendrickson, G. Khitrova, H. M. Gibbs, G. Rupper, C. Ell, O. B. Shchekin, D. G. Deppe, Vacuum Rabi splitting with a single quantum dot in a PC nanocavity. *Nature* 432, 200-203 (2004).
7. Y. Akahane, T. Asano, B.-S. Song, S. Noda, High-Q photonic nanocavity in a two-dimensional PC. *Nature* 425, 944-947 (2003).
8. R. Chikkaraddy, B. de Nijs, F. Benz, B. Felix, S. J. Barrow, O. A. Scherman, E. Rosta, A. Demetriadou, P. Fox, O. Hess, J. J. Baumberg, Single-molecule strong coupling at room temperature in plasmonic nanocavities. *Nature* 535, 127-130 (2016).
9. C. Sauvan, J. P. Hugonin, I. S. Maksymov, P. Lalanne, Theory of the spontaneous optical emission of nanosize photonic and plasmon resonators. *Phys. Rev. Lett.* 110, 237401 (2013).
10. G. M. Akselrod, C. Argyropoulos, T. B. Hoang, C. Ciraci, C. Fang, J. Huang, D. R. Smith, M. H. Mikkelsen, Probing the mechanisms of large Purcell enhancement in plasmonic nanoantennas. *Nat. Photonics* 8, 835-840 (2014).
11. K. J. Russell, T.-L. Liu, S. Cui, E. L. Hu, Large spontaneous emission enhancement in plasmonic nanocavities. *Nat. Photonics*. 6, 459-462 (2012).
12. C. Junge, D. O'Shea, J. Volz, A. Rauschenbeutel, Strong coupling between single atoms and nontransversal photons. *Phys. Rev. Lett.* 110, 213604 (2013).
13. O. Benson, Assembly of hybrid photonic architectures from nanophotonic constituents. *Nature* 480, 193-199 (2011).

14. M. K. Dezfouli, R. Gordon, S. Hughes, Modal theory of modified spontaneous emission of a quantum emitter in a hybrid plasmonic photonic-crystal cavity system. *Phys. Rev. A.* 95, 013854 (2017).
15. H. Lian, Y. Gu, J. Ren, F. Zhang, L. Wang, Q. Gong, Efficient Single Photon Emission and Collection Based on Excitation of Gap Surface Plasmons. *Phys. Rev. Lett.* 114, 193002 (2015).
16. J. Ren, Y. Gu, D. Zhao, F. Zhang, T. Zhang, Q. Gong, Evanescent-Vacuum-Enhanced Photon-Exciton Coupling and Fluorescence Collection. *Phys. Rev. Lett.* 118, 073604 (2017).
17. H. J. Kimble, The quantum internet. *Nature* 453, 1023-1030 (2008).
18. J. Petersen, J. Volz, A. Rauschenbeutel, Chiral nanophotonic waveguide interface based on spin-orbit interaction of light. *Science* 346, 67-71 (2014).
19. S. Mahmoodian, K. Prindal-Nielsen, I. Söllner, S. Stobbe, and P. Lodahl, Engineering chiral light-matter interaction in PC waveguides with slow light. *Opt. Mater. Express.* 7, 43-51 (2017).
20. S.-H. Gong, F. Alpegiani, B. Sciacca, E. C. Garnett, L. Kuipers, Nanoscale chiral valley-photon interface through optical spin-orbit coupling. *Science* 359, 443-447 (2018).
21. F. J. Rodríguez-Fortuño, G. Marino, P. Ginzburg, D. O'Connor, A. Martínez, G. A. Wurtz, A. V. Zayats, Near-Field Interference for the Unidirectional Excitation of Electromagnetic Guided Modes. *Science* 340, 328-330 (2013).
22. L. Marrucci, Quantum optics: Spin gives direction. *Nat. Phys.* 11, 9-10 (2014).

23. P. Lodahl, S. Mahmoodian, S. Stobbe, A. Rauschenbeutel, P. Schneeweiss, J. Volz, H. Pichler, P. Zoller, Chiral quantum optics. *Nature* 541, 473480 (2017).
24. A. B. Young, A. C. T. Thijssen, D. M. Beggs, P. Androvitsaneas, L. Kuipers, J. G. Rarity, S. Hughes, R. Oulton, Polarization Engineering in PC Waveguides for Spin-Photon Entanglers. *Phys. Rev. Lett.* 115, 153901 (2015).
25. C. Gonzalez-Ballester, A. Gonzalez-Tudela, F. J. Garcia-Vidal, E. Moreno, Chiral route to spontaneous entanglement generation. *Phys. Rev. B* 92, 155304 (2015).
26. I. Söllner, S. Mahmoodian, S. L. Hansen, L. Midolo, A. Javadi, G. Kiršanskė, T. Pregnolato, H. El-Ella, E. H. Lee, J. D. Song, S. Stobbe, P. Lodahl, Deterministic photon-emitter coupling in chiral photonic circuits. *Nat. Nanotechnol.* 10, 775-778 (2015).
27. T. C. Ralph, I. Söllner, S. Mahmoodian, A. G. White, P. Lodahl, Photon Sorting, Efficient Bell Measurements, and a Deterministic Controlled- Z Gate Using a Passive Two-Level Nonlinearity. *Phys. Rev. Lett.* 114, 173603 (2015).
28. I. Shomroni, S. Rosenblum, Y. Lovsky, O. Bechler, G. Guendelman, B. Dayan, All-optical routing of single photons by a one-atom switch controlled by a single photon. *Science* 345, 903-906 (2014).
29. C. Sayrin, C. Junge, R. Mitsch, B. Albrecht, D. O'Shea, P. Schneeweiss, J. Volz, A. Rauschenbeutel, Nanophotonic optical isolator controlled by the internal state of cold atoms. *Phys. Rev. X* 5, 041036 (2015).
30. M. Scheucher, A. Hilico, E. Will, J. Volz, A. Rauschenbeutel, Quantum optical circulator controlled by a single chirally coupled atom. *Science* 354, 1577-1580 (2016).

31. P. Lodahl, S. Mahmoodian, S. Stobbe, Interfacing single photons and single quantum dots with photonic nanostructures. *Rev. Mod. Phys.* 87, 347-400 (2015).
32. B. le Feber, N. Rotenberg, L. Kuipers, Nanophotonic control of circular dipole emission. *Nat. Commun.* 6, 6695 (2015).
33. R. J. Coles, D. M. Price, J. E. Dixon, B. Royall, E. Clarke, P. Kok, M. S. Skolnick, A. M. Fox, M. N. Makhonin, Chirality of nanophotonic waveguide with embedded quantum emitter for unidirectional spin transfer. *Nat. Commun.* 7, 11183 (2016).
34. M. Arcari, I. Söllner, A. Javadi, S. L. Hansen, S. Mahmoodian, J. Liu, H. Thyrrstrup, E. H. Lee, J. D. Song, S. Stobbe, P. Lodahl, Near-unity coupling efficiency of a quantum emitter to a photonic-crystal waveguide. *Phys. Rev. Lett.* 113, 093603 (2014).
35. D. O'Connor, P. Ginzburg, F. J. Rodríguez-Fortuño, G. A. Wurtz, A. V. Zayats, Spin-orbit coupling in surface plasmon scattering by nanostructures. *Nat. Commun.* 5, 5327 (2014).
36. H. J. Carmichael, *Statistical Methods in Quantum Optics 2*, Springer-Verlag Berlin Heidelberg (2008).
37. T. K. Hakala, J. J. Toppari, A. Kuzyk, G. Khitrova, H. M. Gibbs, G. Rupper, C. Ell, O. B. Shchekin, D. G. Deppe, Vacuum Rabi splitting and strong-coupling dynamics for surface-plasmon polaritons and rhodamine 6G molecules. *Phys. Rev. Lett.*, 103, 053602 (2009).
38. M. D. Birowosuto, A. Yokoo, G. Zhang, K. Tateno, E. Kuramochi, H. Taniyama, M. Takiguchi, M. Notomi, Movable high-Q nanoresonators realized by semiconductor nanowires on a Si PC platform. *Nat. Mater.* 13, 279-285 (2014).

39. R. Mitsch, C. Sayrin, B. Albrecht, P. Schneeweiss, A. Rauschenbeutel, Quantum state-controlled directional spontaneous emission of photons into a nanophotonic waveguide. *Nat. Commun.* 5, 5713 (2014).
40. P. B. Johnson, R. W. Christy, OPTICAL CONSTANTS OF NOBLE METALS. *Phys. Rev. B* 6, 4370 (1972).
41. K. Słowik, R. Filter, J. Straubel, F. Lederer, C. Rockstuhl, Strong coupling of optical nanoantennas and atomic systems. *Phys. Rev. B* 88, 195414 (2013).
42. A. B. Evlyukhin, G. Brucoli, L. Martín-Moreno, S. I. Bozhevolnyi, F. J. García-Vidal, Surface plasmon polariton scattering by finite-size nanoparticles. *Phys. Rev. B* 76, 075426 (2007).
43. N. Lukas, H. Bert, *Principles of nano-optics*, Cambridge university press, (2012).
44. M. O. Scully, M. S. Zubairy, *Quantum Optics*, Cambridge University Press (2006).
45. J. R. Johansson, P. D. Nation, F. Nori, QuTiP 2: A Python framework for the dynamics of open quantum systems. *Comput. Phys. Commun.* 184, 1234-1240 (2013).
46. A. Ridolfo, O. Di Stefano, N. Fina, R. Saija, S. Savasta, Quantum Plasmonics with Quantum Dot-Metal Nanoparticle Molecules: Influence of the Fano Effect on Photon Statistics. *Phys. Rev. Lett.* 105, 263601 (2010).